

Influence of Ag Doping on Physico-Chemical Properties of the $\text{Ge}_{28}\text{Sb}_{12}\text{Se}_{60}$ Chalcogenide Glassy Matrix

Deepak Patil^{1, 2}, Manisha Konale¹, Lukas Strizik¹, Laurent Calvez³, David Le Coq³, Bozena Frumarova⁴, Milan Vlcek⁴ and Tomas Wagner^{1*}

1. Department of General and Inorganic Chemistry and CEMNAT, Faculty of Chemical Technology, University of Pardubice, Studentska 95, Pardubice, 53210, Czech Republic

2. Current Affiliation- School of Mechanical and Materials Engineering, Washington State University, Pullman, WA - 99164, USA

3. Institut des Sciences Chimiques de Rennes, Eq. Verres et Céramiques, UMR 6226 CNRS, Université de Rennes1, 35042 Rennes Cedex, France

4. Institute of Macromolecular Chemistry of Czech Academy of Sciences, v.v.i., Heyrovského nam. 2, 162 06 Prague, Czech Republic

Abstract: Thermal, optical and electrical properties of the $\text{Ag}_x(\text{Ge}_{28}\text{Sb}_{12}\text{Se}_{60})_{100-x}$ system (for $x = 0$ to 20) are systematically studied using various characterization techniques. In the present study, we have shown the reproducibility of the current results with the previously published literature and several novel results are also presented. The impedance data for the understanding of electrical properties of the materials has been analyzed using the random-walk (RW) model. We observed that, Ag playing two different concentration dependent roles i.e. above and below the 5% of Ag concentration, which is confirmed by the Raman analysis. The anomalous behaviors of electrical conductivity, optical and thermal properties with increasing Ag concentrations are explained by the role of Ag in the structural modification. We compared the diffusion coefficient (D), obtained from the RW model analysis with the experimental data (obtained from tracer diffusion) and found diffusion coefficient (D), obtained from the RW model are in good agreement corresponded with the experimental values. We also found a major change in conductivity of insulating $\text{Ge}_{28}\text{Sb}_{12}\text{Se}_{60}$ ($\sim 10^{-14} \text{ S}\cdot\text{cm}^{-1}$) to a fast ionic conductor for $\text{Ag}_{15}(\text{Ge}_{28}\text{Sb}_{12}\text{Se}_{60})_{85}$ ($\sim 10^{-6} \text{ S}\cdot\text{cm}^{-1}$), i.e., a nine orders of magnitude. We demonstrated that the random-walk model can replace a time consuming and expensive tracer diffusion method for the determination of D. The present article helps to understand the ion conduction mechanism in disordered / amorphous materials.

Key words: Chalcogenide glasses, density, impedance spectroscopy, random-walk model, diffusion coefficient, tracer diffusion method.

1. Introduction

Chalcogenide glasses are widely studied due to their unique properties, such as the high nonlinear refractive index, low phonon energy, from visible to mid-IR transparency and low bandgap, when compared with their corresponding crystalline as well as glassy oxide counterparts [1]. It represents chalcogenide glasses as a potential candidate material for the IR optical devices, optical fiber, waveguide, phase change memory, bio-chemical sensors, etc.

[2-5].

We selected the $\text{Ge}_{28}\text{Sb}_{12}\text{Se}_{60}$ glassy matrix as a base/mother matrix, since the $\text{Ge}_{28}\text{Sb}_{12}\text{Se}_{60}$ material is well known homogeneous bulk glasses, commercialized by Vitron under the reference IG5[®] [6], and Ge-Sb-Se is commercialized under the reference name AMTIR3[®] by Amorphous Materials Inc. [7], which indicates the commercial importance of the materials under study.

Chalcogenide glasses are a class of vitreous semiconductors, having usually the p-type conductivity [8]. Chalcogenide glasses doped with a metal such as Ag, Cu, Li, Na and/or their corresponding halides, i.e., AgI, LiI, etc., can act as

*Corresponding author: Tomas Wagner, professor, research fields: amorphous chalcogenide materials for switching devices and solid state battery.

ionic conductors or even fast ionic conductors with $\sigma > 10^{-7} \text{ S}\cdot\text{cm}^{-1}$ [8, 9]. This presents them as a candidate for solid state batteries, ionic memories and many electronic devices [3, 9, 10]. Even though alkali metal-doped (especially Li-doped) chalcogenide glasses show high current density, high ionic conductivity, but they are highly unstable in a humid environment and are problematic regarding safety. Cu-doped chalcogenides show lower ionic conduction than those with an equal amount of Ag-doped corresponding chalcogenide matrix. This creates Ag-doped chalcogenides as a potential candidate for solid state electrolytes for future energy-storing materials and for the other ion conductor material applications.

Ionic conductors have been studied for many years; nevertheless, the mechanism of ion conduction is still not well understood [11]. As the microstructure and dynamics of ions controls the electrical and other properties of the materials, it is important to study and correlate the structural and dynamics properties of the materials.

To understand the dynamic of ions, it is necessary to study the diffusion coefficient of the material. The diffusion coefficient is usually studied experimentally by the tracer diffusion method, or calculated theoretically or using a computational study [12, 13]. As the tracer diffusion technique is very expensive (due to the use of a radioactive element) and time consuming (even more than 3 months are required for one experiment in a low diffusion coefficient material), it is inconvenient for commercial use [12].

We studied the structural, thermal and optical properties of $\text{Ag}_x(\text{Ge}_{28}\text{Sb}_{12}\text{Se}_{60})_{100-x}$ using XRD (X-ray diffraction), SEM (Scanning electron microscopy), EDS (Energy dispersive spectroscopy), Raman, IR (Infra-red) spectroscopy, UV-Vis (Ultra-violet visible spectroscopy), DSC (Differential scanning calorimetry) etc. The electrical properties of the materials were studied using IS (Impedance spectroscopy) and the IS data were analyzed using a

model – recently developed by our group – called a random-walk (RW) model [13, 14]. As stated in our recent articles [14-16], the RW model introduces several benefits when compared with the conventional EEC (Equivalent electric circuit) analysis, such as RW model can calculate physical parameters (density of mobile ions N_{ions} , diffusion coefficient D , hopping time of ions etc., quantitatively) and do not need of an equivalent electric circuit. The detail about RW model and EEC model were already described elsewhere [14-16]. We compared the diffusion coefficient (D), obtained by the RW model analysis, with the experimentally obtained value from tracer diffusion method. This comparison of parameters obtained by RW analysis with the tracer diffusion results validates the parameters obtained using the RW model; it also promises valuable applications for a future researcher to determine D without using the expensive and tedious tracer diffusion method, which is one of the important aim of this article. We also tried to correlate the structural and electrical properties of the materials, which provides the more detail understanding of the correlation between structural changes and dynamics of ions.

2. Experimental Methods

The samples having composition $\text{Ag}_x(\text{Ge}_{28}\text{Sb}_{12}\text{Se}_{60})_{100-x}$ with $0 \leq x \leq 20$, were prepared by the conventional melt quenching method. All the elements (Ag, Ge, Sb and Se) used for the synthesis were of high purity 5 N. A batch of 10 g, with an appropriate amount of each element was sealed in a quartz ampoule with the inner diameter of 10 mm under high vacuum (10^{-3} Pa). The mixture was heated in a rocking furnace at temperature up to 950°C with a rate $2^\circ\text{C}/\text{min}$ and dwell at 950°C for 12 h in the rocking furnace, before being slowly cooled down to 730°C . The ampoule was then quenched in water and annealed at temperature 10°C lower than T_g for 4 h, finally cooled down slowly to the room temperature to minimize the inner tension. The obtained glass rods

were sliced into disks of 10 mm in diameter and thickness of around 1-2 mm. The disks were then polished with optical quality. The polished disks were also used for electrical measurement with gold sputtered on both sides of the disks for a good electrical contact with the electrodes.

The optical transmittance window of each glass was characterized using a UV-VIS double beam CARY spectrometer with a transmission precision of $\pm 2\%$ and a Bomem-Fourier transform IR spectrometer with the transmission precision of $\pm 2\%$. Differential scanning calorimetry (DSC Perkin-Elmer Pyris 1) with the heating rate $10\text{ }^{\circ}\text{C}\cdot\text{min}^{-1}$ was used for measuring the characteristic temperatures of the glassy systems. The density of each glass was measured by the Archimedes method using ethanol as the immersion fluid on a Mettler Toledo XS64 balance. The determination of crystalline and amorphous nature was performed using the XRD analysis with D8 – advance with a Cu anode in the angle range of $2\theta = 10\text{--}80^{\circ}$ with step 0.02° . The Raman analysis was done using a FT-IR IFS 55 Bruker spectrometer equipped with a Raman module FRA 106. Raman spectra were obtained using a Nd-YAG laser with the excitation wavelength $\lambda = 1,064\text{ nm}$ and output power 50 mW. The refractive index and optical bandgap (E_g) were measured using a variable angle ellipsometric spectroscopy (VASE) J. A. Woollam Co., with an automatic rotating-analyzer (with a spectral range 300-2,300 nm, angles of incidence 60° , 65° and 70°) and data analysis was performed using the Tauc-Lorentz model. Surface morphology was studied by SEM. The elemental analysis was characterized by an EDS spectrometer.

Electrical properties were analyzed using IS, carried out on a PGSTAT 302N with the FRA32 and NOVA 10 software. The cell used stainless disk-like electrodes sputtered with gold to block the Ag^+ ions passage. Temperature dependence IS being carried out in the range from 298 K to 368 K with a frequency range from 1 Hz to 50 KHz; The temperature was

controlled with a Microcell HC set-up (Rhé instruments).

3. Results and Discussion

All prepared samples look shiny dark black in color. Fig. 1 shows the case example of $\text{Ag}_{15}(\text{Ge}_{28}\text{Sb}_{12}\text{Se}_{60})_{85}$; It shows even after 15% of Ag doping, the sample still obtained in a nice shiny glassy rod.

The prepared samples represented namely by G0 to G9, as given in Table 1 with their corresponding chemical compositions.

3.1 XRD Analysis

The quality of the glasses was examined using X-ray SEM.

From the XRD analysis presented in Fig. 2, all samples show an amorphous nature except for the G9

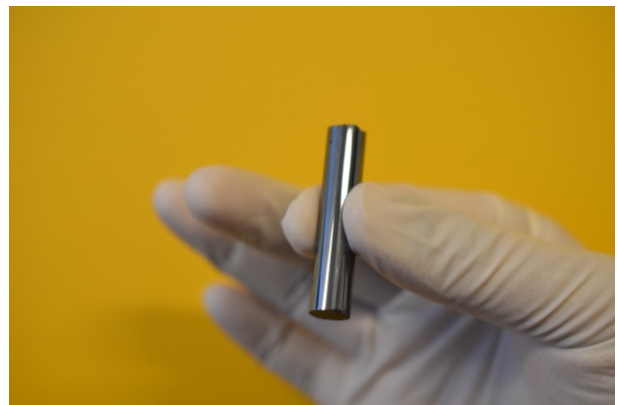


Fig. 1 An image of $\text{Ag}_{15}(\text{Ge}_{28}\text{Sb}_{12}\text{Se}_{60})_{85}$ glassy sample rod of 10 mm in diameter.

Table 1 Notations of the samples with their corresponding compositions.

Sample Name	Sample Composition
G0	$\text{Ge}_{28}\text{Sb}_{12}\text{Se}_{60}$
G1	$\text{Ag}_{0.2}(\text{Ge}_{28}\text{Sb}_{12}\text{Se}_{60})_{99.8}$
G2	$\text{Ag}_{0.4}(\text{Ge}_{28}\text{Sb}_{12}\text{Se}_{60})_{99.6}$
G3	$\text{Ag}_{0.6}(\text{Ge}_{28}\text{Sb}_{12}\text{Se}_{60})_{99.4}$
G4	$\text{Ag}_{0.8}(\text{Ge}_{28}\text{Sb}_{12}\text{Se}_{60})_{99.2}$
G5	$\text{Ag}_1(\text{Ge}_{28}\text{Sb}_{12}\text{Se}_{60})_{99}$
G6	$\text{Ag}_5(\text{Ge}_{28}\text{Sb}_{12}\text{Se}_{60})_{95}$
G7	$\text{Ag}_{10}(\text{Ge}_{28}\text{Sb}_{12}\text{Se}_{60})_{90}$
G8	$\text{Ag}_{15}(\text{Ge}_{28}\text{Sb}_{12}\text{Se}_{60})_{85}$
G9	$\text{Ag}_{20}(\text{Ge}_{28}\text{Sb}_{12}\text{Se}_{60})_{80}$

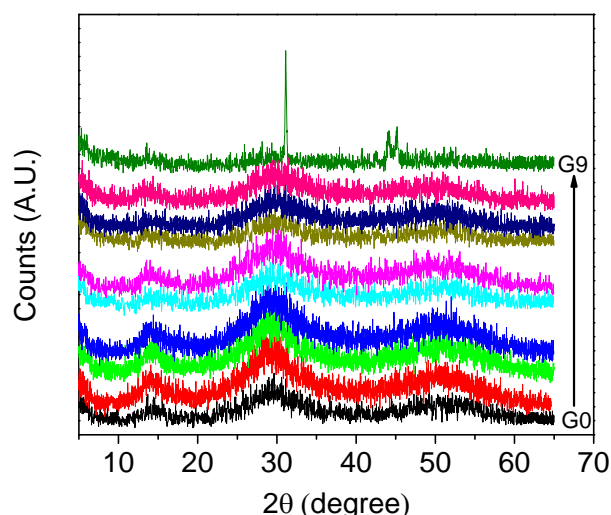


Fig. 2 The XRD plot of the G0 to G9 samples.

sample. In fact, in the case of $\text{Ag}_{20}(\text{Ge}_{28}\text{Sb}_{12}\text{Se}_{60})_{80}$, from Fig. 2, the sample is found crystalline in nature, probably containing GeSe_2 and Sb_2Se_3 crystalline phases (the detail study on crystalline phases were not done in the present study).

3.2 Surface Morphology and Elemental Analysis:

For the confirmation of homogeneity of the sample, we examined prepared samples under SEM (not shown Figs. here) and elemental analysis done by EDS shown in Fig. 3. Surprisingly from the SEM analysis, the topology/morphology of the sample G9 doesn't show any crystalline features, which means the sample is not fully crystalline but it may contain nano/micro crystallites. From the XRD analysis and SEM, it is also clear that the samples from G0 to G8, i.e., 0 to 15% Ag-doped are in the amorphous nature, while further increase of Ag concentration i.e. > 15 %, it tends to induce crystallization in the base matrix. It means that the saturation limit of Ag doping in $\text{Ag}_x(\text{Ge}_{28}\text{Sb}_{12}\text{Se}_{60})_{100-x}$ sample is less than 20% (off course this saturation limit can vary, depending upon the preparation conditions, such as the reaction temperature, i.e., at what temperature the melt is quenched, quenching rate etc.).

From the EDS analysis as shown in Fig. 3, the glass compositions are in reasonable agreement with the theoretical values, except there is a small deviation in

the sample G4 (which may be due to the sample handling during preparation).

3.3 Density Study

The densities of all prepared samples were measured using the Archimedes principle. The obtained density of each sample is shown in Fig. 4.

We observed that the density increased from $4.66 \text{ g}\cdot\text{cm}^{-3}$ to $5.48 \text{ g}\cdot\text{cm}^{-3}$ as the Ag concentration changed from 0 to 15% respectively. Fig. 4 clearly shows that the density does not exactly increases linearly with the Ag concentrations. This non-linear behavior as well as all the density values gives good agreement with results obtained by Bychkov, et al. [12].

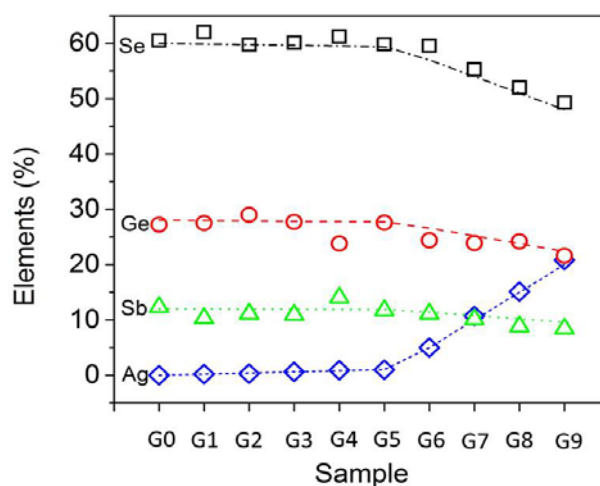


Fig. 3 The EDS analysis of a prepared sample. The open symbol represents the actual atomic percent of elements and the dotted lines represent the theoretical values.

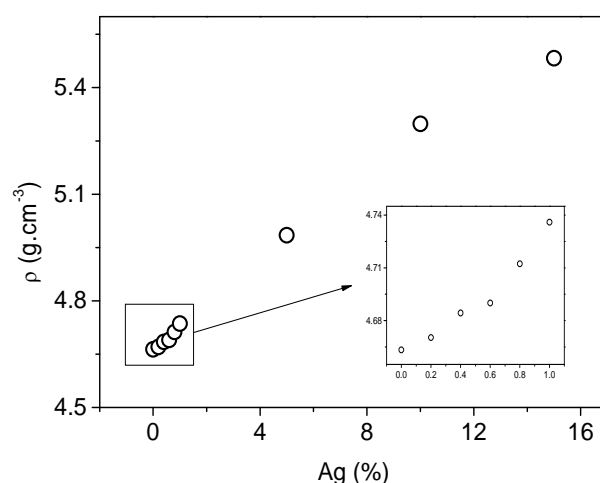


Fig. 4 Density as a function of Ag atomic percent. Inset displays a magnified image of the low Ag content.

From the density measurement we calculated the mean atomic volume and Ag-Ag atomic distance ($r_{\text{Ag-Ag}}$) using the following Eqs. (1) and (2), respectively,

$$\text{Mean atomic volume} = \frac{M}{\rho \times N_f} \quad (1)$$

where, M is the molecular weight of the sample, ρ is the density and N_f is the number of atoms in a formula unit.

The atomic distance $r_{\text{Ag-Ag}}$ was calculated using the following equation:

$$r_{\text{Ag-Ag}} = \frac{1}{(N)^{\frac{1}{3}}} \quad (2)$$

where, N is the number of Ag atoms in cm^{-3} . The obtained results shown graphically in Figs. 5 and 6, respectively. Mean atomic volume and mean atomic distances are also in good agreement the earlier results of Bychkov, et al. [12].

In Fig. 6, the mean atomic distance shows the nonlinear decreasing behavior. It is also clearly observing that, the two slopes (one at for lower Ag concentrations and other at for higher Ag concentrations) of the decrease of the mean atomic volume as a function of the Ag concentration, implying two different concentrations dependent behavior of the Ag. Inset displays a magnified image

of the lower Ag concentration samples, which gives a clear curved nature of the mean atomic volume as a function of the Ag concentrations.

This decreasing behavior of in the mean atomic volume indicates that the addition of Ag concentration lower than 1% creates more disorder in structure, i.e., total volume expansion, i.e., density decrease, which is consistent with the density results shown in Fig. 4, as for the low Ag content ($\leq 1\%$) slower increase of density with the addition of Ag. For the higher content of Ag ($\geq 1\%$), the average atomic volume decreased more rapidly, indicating that the less modification in the structure, the added Ag more than 1% are mostly occupying empty space, i.e. host-guest or lock and key model like behavior. This is also consistent with the density observation, i.e., rapid increase of the density. This dual behavior of Ag may be due to the percentage of weak bonds present in the structure, i.e., the base matrix structure ($\text{Ge}_{28}\text{Sb}_{12}\text{Se}_{60}$) contains almost 1% of weak bonds, which can easily modify by the Ag. This is further confirmed by the electrical properties and Raman analysis in the later sections.

Fig. 6 shows that the Ag-Ag atomic distance ($r_{\text{Ag-Ag}}$) decreased nonlinearly as the Ag concentration increased from G1 to G8. This may be the reason behind the anomalous behavior of the diffusion coefficient of such ionic materials; we will discuss this finding in greater detail in the later section.

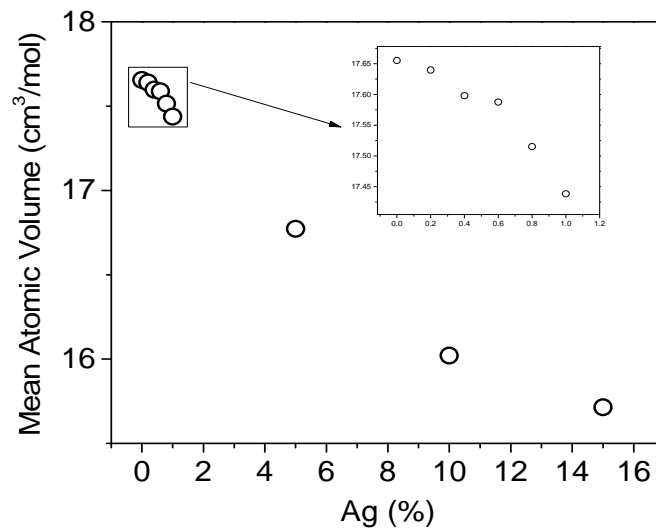


Fig. 5 The mean atomic volume as a function of Ag atomic percent. Inset displays a magnified image of the low Ag content.

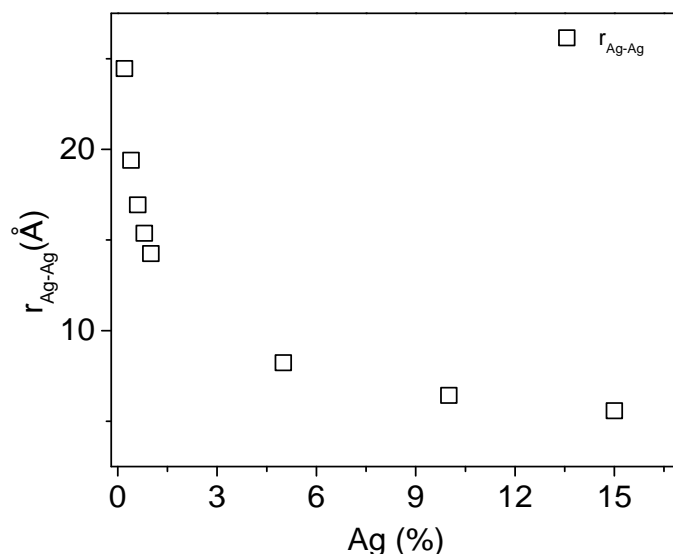


Fig. 6 The Ag-Ag atomic distance distribution as a function of Ag atomic content.

3.4 Thermal Analysis

Using the DSC analysis, we measured the glass transition temperatures (T_g) of all prepared glasses (Fig. 7).

From Fig. 7, it is clear that T_g decreases with the increase of Ag concentration. T_g decreased more than 80 °C as Ag concentration changes from 0 to 15%. From Fig. 7, T_g of the glasses reveals an observable decrease in the T_g , even at 0.2% of the Ag addition and such decrease in T_g continued exponentially in all prepared samples. This supports our earlier comment that, Ag in low concentrations ($\leq 1\%$) modifies the structure, i.e. the breaking of bonds (more detail will discuss in Raman analysis section), but if we further increased the Ag concentration, as stated previously, Ag started to insert in empty space without major modification in structure. All these results are consistent with the density as well as mean atomic volume changes. These changes are further confirmed by the Raman analysis, discussed below. At this point, we would like to mention that no crystallization peak was observed in the temperature 150 °C above T_g , except for G8 and G9. In the case of G8 and G9, we observed the crystallization peak $\sim (T_g + 125\text{ °C})$. The type of glasses which did not show the crystallization peak in the temperature range $\sim (T_g + 150\text{ °C})$, we

considered it as a stable glass, and from the G8, G9 behavior we also understand that the glass stability slowly decreased with increasing the Ag concentration. The glasses with such low tendency to crystallize are promising for drawing optical fiber [17].

3.5 Optical Study

3.5.1 UV-VIS Near IR Measurement

The measured optical transparencies of the prepared glasses in the near IR region were shown in Fig. 8. All the glasses were transparent in near-IR; the transparency decreased from 68% to 50% in a sequence from G0 to G8 respectively. In the Table 2, given the thickness of the samples, used for optical measurements.

The decrease in transparency (shown in Fig. 8) is consistent with the densification of the sample by the addition of Ag. We also observed that the absorption wavelength point shifted from 0.8 μm to 1 μm as the Ag content increased from 0 to 15%, which we can clearly see in the inset image of Fig. 8. As we know that the chalcogenide glass transmission limited to shorter wavelength (as shown in Fig. 8) due to electronic transition by the optical absorption from valence to conduction band [18, 19]. From Fig. 8, the shift of wavelength from 0.8 μm to 1 μm indicating that the addition of Ag, decreasing optical bandgap,

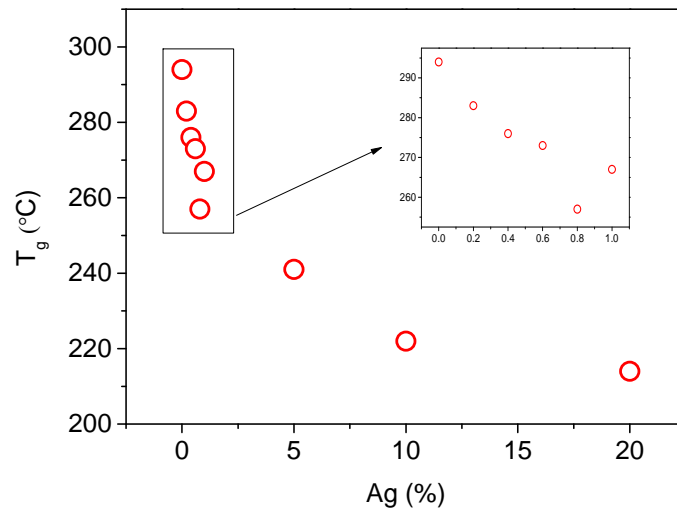


Fig. 7 Glass transition temperature (T_g) of the prepared glasses as a function of Ag%. Inset displays a magnified image of the low Ag content.

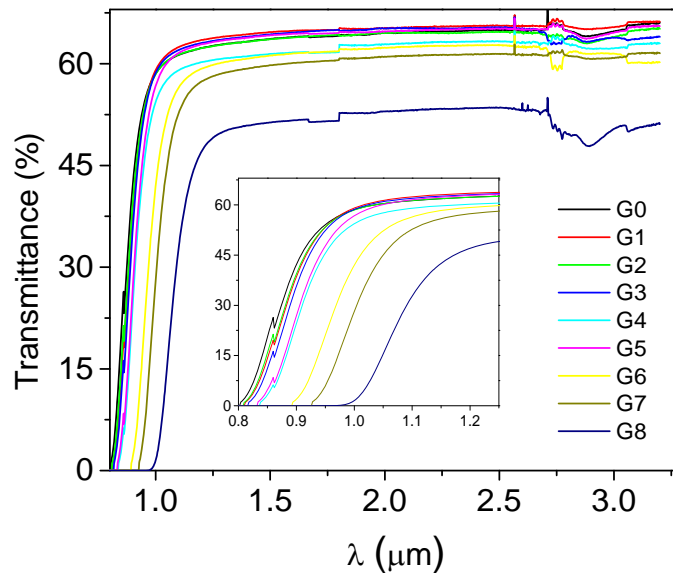


Fig. 8 The optical transmission spectrum of prepared glasses in the near-IR region. Inset displays a magnified image in the lower wavelength region.

Table 2 Sample name and the corresponding thickness.

Sample name	Thickness (mm)
G0	1.5
G1	1.18
G2	1.02
G3	0.89
G4	0.75
G5	1.26
G6	0.86
G7	0.88
G8	1.39

would be further confirmed from ellipsometric studies.

3.5.2 Ellipsometric Study

Using the variable angle ellipsometric measurements, we calculated the refractive index (n) as a function of wavelength (not shown here). At low Ag concentration (up to 1%), the refractive index value scattered, but at higher concentration ($\geq 1\%$) the refractive indices increased, and at higher Ag concentration $\sim (\geq 15\%)$ showing the saturation behavior, which we can observe in Fig. 9, where refractive indices at $1.55 \mu\text{m}$ were plotted against the Ag concentration. Using the ellipsometric measurement we also calculated the bandgap energy

(E_g) of each glass from G0 to G8. The obtained E_g first scattered in a low Ag concentration sample, but in the case of higher Ag concentration, it decreased linearly as shown in Fig. 10, i.e., the red shift occurred due to the addition of Ag. This decrease of E_g from 1.79 eV to 1.41 eV with the Ag concentration changed from 0 to 15% respectively, is consistent with the shift observed in Fig. 8. This scattering behavior in low concentration due to deviation of sample composition by experimental error i.e. in such low concentrated Ag sample, even very small deviation in composition will give very large effect on final results (for ex. 0.1 mg

deviation in 1 mg will give 10 % deviation, while 0.1 mg deviation in 1 g will give only 0.01 % deviation).

3.6 Impedance Analysis

The electrical properties of the prepared glasses were determined using impedance spectroscopy (IS). We measured the impedance of each glass from 298 K to 368 K, most of the glasses (especially with a lower content of Ag, i.e. $\leq 1\%$) show lower conductivity than $10^{-11} \text{ S}\cdot\text{cm}^{-1}$ at 298 K, which is outside the limit of our impedance instrument. For the same reason, comparing the electrical conductivity of all the samples,

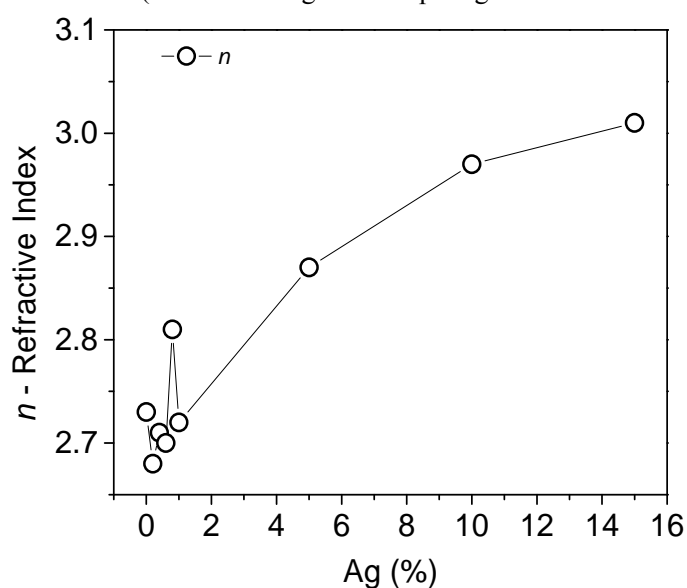


Fig. 9 The refractive index at 1.55 μm as a function of the Ag content.

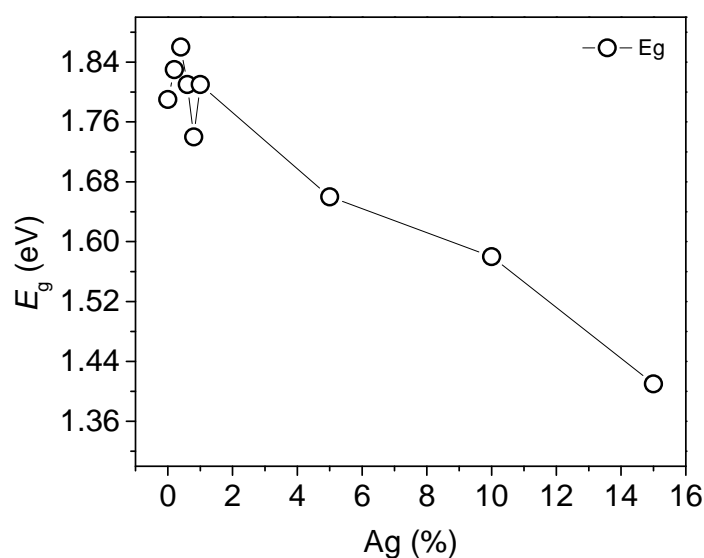


Fig. 10 The optical bandgap E_g as a function of Ag atomic percent. The solid line represents the guideline for the eye.

we have shown the resistivity plot (ρ_1, ρ_2) at 368 K, in Figs. 11a and 11b. The real and imaginary parts of the resistivity, ρ_1 and ρ_2 , respectively, were deduced from the $Z_1 - Z_2$ data taking into account the dimensions of the sample:

$$\begin{aligned}\rho_1 &= \frac{Z_1 A}{L} \\ \rho_2 &= \frac{Z_2 A}{L}\end{aligned}\quad (3)$$

where A is the surface area of an electrode and L is sample thickness). For the sample G0, the conductivity even at 368 K was still beyond the limit of instrument measurement, not shown in Fig. 11. Indeed, the dispersion of the points in the Nyquist's plot for G1 sample can be attributed to this limitation. As shown in Fig. 11a and 11b, the impedance of the

glasses systematically decreased with the increase of Ag content. It is worth to noting that even at 15% of Ag, i.e., G8 at 368 K did not show any electrode polarization phenomena, i.e., tail, which is generally observe in similar ionic conductors [8]. This is further confirmed by the real (σ_1) and imaginary (σ_2) part of the conductivity as a function of angular frequency (ω) shown in Figs. 12a and 12b. The real and imaginary parts of the conductivity σ_1 and σ_2 were calculated according to the equations

$$\begin{aligned}\sigma_1 &= \frac{\rho_1}{\rho_1^2 + \rho_2^2} \\ \sigma_2 &= \frac{\rho_2}{\rho_1^2 + \rho_2^2}\end{aligned}\quad (4)$$

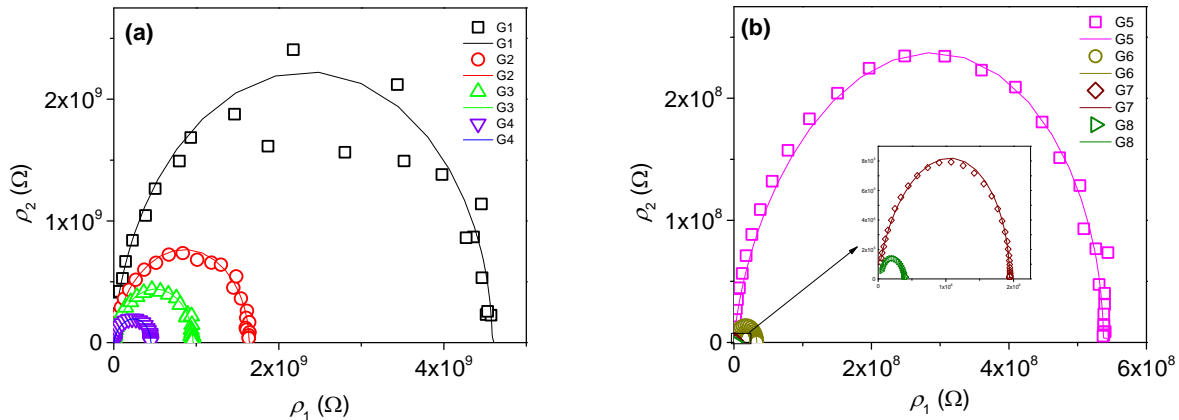


Fig. 11 The real part of resistivity (ρ_1) vs the imaginary part of resistivity (ρ_2) as a function of the sample composition at 368 K, (a) from G1 to G4 and (b) G5 to G8 (inset displays a magnified image of G7 and G8). Open symbols represent the experimental data where as solid line represents the RW model fitting.

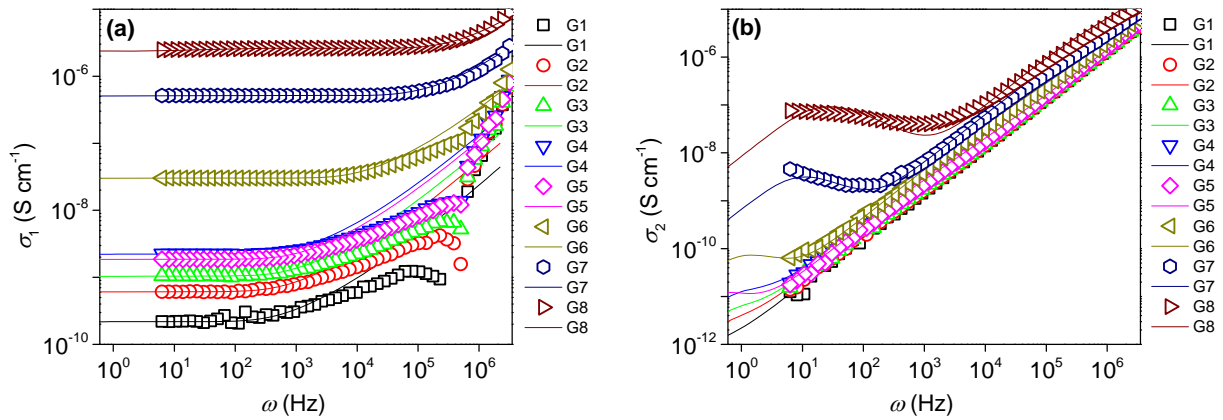


Fig. 12 (a) The real part of conductivity σ_1 and (b) the imaginary part of conductivity σ_2 as a function of the sample composition at 368 K. Open symbols represent the experimental data where as solid line represents the RW model fitting.

In Fig. 12a, the constant plateau in the mid-frequency region represents the dc-conductivity $\sigma(0)$ corresponding to the total conductivity (ionic + electronic), increases with Ag concentration, while the loss conductivity (increasing behavior of conductivity as a function of frequency) in high frequency region ($\sim 10^3$ Hz) shifts to further high frequency side with the Ag content increases ($\sim 10^5$ Hz as in the case of G8). In loss conductivity part in the high frequency region, there is a distortion in behavior (scattering and the instead of increasing behavior as a function of frequency decreasing behavior at certain frequencies) of data in a high resistance sample, which is from an instrumental error. This error was further confirmed by connecting resistance of 100 M Ω and 4 nF capacitance in a parallel way and measuring the impedance: a similar distortion was found in the high frequency part of σ_1 . In all cases no electrode polarization phenomena was observed, i.e., no bending observed in the low frequency side in the measured frequency region of σ_1 . This was also confirmed by the imaginary part of conductivity σ_2 as shown in Fig. 12b, where no hump was observed in the low frequency region [14, 15], while the onset of electrode polarization was observed in a higher Ag content ($\geq 5\%$), i.e., upward bending in the near mid-frequency region and shifts towards a high frequency side as Ag increased. This confirms the presence of ionic conductivity contribution in the sample, but the ionic conductivity contribution is not enough to make a barrier layer as a full electrode polarization. This may be because of the presence of lone pairs of Se, which highly contributes to the electronic conductivity in the total conductivity [12]. This high electronic contribution helps to reduce the mobile ion (Ag^+ to Ag) before reaching the electrode interface and inhibits the electrode polarization effect. Even though the ionic conduction was lower in comparison with a corresponding sulfur-based chalcogenide having an equal amount of Ag atomic

percent [12], conductivity still increased in the scope of five orders of magnitude from $2.2 \times 10^{-10} \text{ S}\cdot\text{cm}^{-1}$ to $2.6 \times 10^{-6} \text{ S}\cdot\text{cm}^{-1}$ as Ag atomic percent increased from 0.2 to 15%. Interestingly, this increase as a function of the Ag content is not linear as shown in Fig. 13, which is consistent with the other authors observations [12, 20]. Fig. 13 shows that the conductivity of prepared glasses at 298 K is lower by one order of magnitude than at 368 K, but the behavior of conductivity as a function of the Ag concentration is still similar. Also, lower Ag concentration ($\leq 1\%$) samples conductivity at 298 K are not presented in Fig. 13 due to their conductivity being out of the instrument limit, but the conductivity of these samples were already measured by Bychkov et al., using the dc-conductivity measurement [12]. They found that the conductivity of the G0 sample was $10^{-14} \text{ S}\cdot\text{cm}^{-1}$, i.e., the conductivity of G8 sample at 368 K in comparison with the conductivity of G0 sample, the conductivity has increased by 9 orders of magnitude. This is a clear evidence of the transformation of insulating material to a fast ionic conducting material ($\sigma \geq 10^{-7} \text{ S}\cdot\text{cm}^{-1}$).

Temperature dependence conductivity plotted as conductivity vs reciprocal of temperature shown in Fig. 14. The $\sigma(0)$ follows the Arrhenius law, given as,

$$\sigma(0) = \sigma_0 e^{-\frac{E_a}{kT}} \quad (5)$$

The activation energy (E_a), shown in Fig. 17, was calculated using the Arrhenius Eq. (5). As shown in Fig. 17, E_a decreased from 0.63 eV to 0.39 eV as Ag increased from 0.8 to 15% respectively. This decrease in activation energy was due to a decrease in the Ag-Ag atomic distance ($r_{\text{Ag-Ag}}$), as shown in Fig. 6.

The ionic conductivity (changed $10^{-14} \text{ S}\cdot\text{cm}^{-1}$ to $10^{-6} \text{ S}\cdot\text{cm}^{-1}$ i.e. by nine orders) and the activation energy decreases to 0.39 eV, all these results are also in reasonable agreement with the Bychkov et al. results [12] and will be discussed more detail later in the following section. This gives the reproducibility of the obtained results.

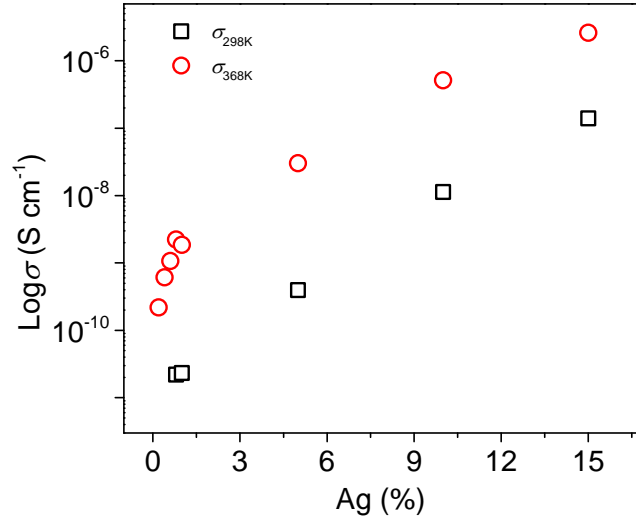


Fig. 13 Conductivity as a function of the Ag content at 298 K and 368 K.

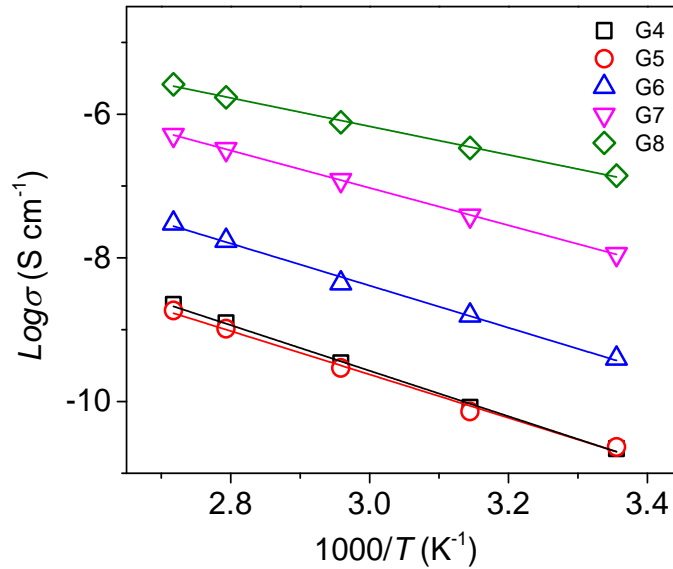


Fig. 14 Conductivity as a function of reciprocal of temperature. The solid line represents the Arrhenius Eq. (5) fitting.

From the RW model fitting with the experimental data (shown in Figs. 11 and 12), we calculated the important physical parameters such as the number of mobile ions (N_{ions}) and the diffusion coefficient (D) using the following Eqs. (6) and (7), shown in Fig. 15.

$$\sigma(0) = \frac{N_{\text{ions}} (eR)^2}{6 kT \tau_m} \quad (6)$$

and

$$D = \frac{R^2}{6 \tau_m} \quad (7)$$

respectively.

where, R and τ_m are the hopping distance (is the

average distance of ions hopped from one site to another site, for reducing the free parameters in the RW model, R is assumed to be constant i.e. 5 \AA) and maximum hopping time (is the maximum time taken by the ion to overcome the highest potential barrier in the matrix) of mobile ions respectively.

The obtained N_{ions} , as shown in Fig. 15a, increased nonlinearly with the Ag content as we expected. Since from the thermal and density results, it is clear that the bond breaking and the increase of disorder took place in the low Ag content ($\leq 1\%$) sample, expecting more number of non-bridging Ge^+ species which helps to increase more N_{ions} (as non-bridging Ge^+ forms by

breaking weak Ge-Ge homopolar bonds and forming Ge^+ and Ge^-), giving more space/path for conduction of mobile ions and our earlier comment from thermal and density analysis found true as it can observe in Fig. 15a, the rapid increase of N_{ions} for low Ag concentrated samples and then the increment slope decrease which also support the dual behavior of the Ag role in GeSbSe matrix. Fig. 15 also shows the diffusion coefficient (D) have two distinct regions, one is $\leq 1\%$ of Ag and the other one is $\geq 1\%$ of Ag containing samples. This nonlinear behavior of diffusion coefficient is consistent with the other authors' observations [12, 20]. This non-linear behavior of Ag diffusion in such amorphous materials are explained by Bychkov et al., [12] considering the percolation behavior in a lower content of Ag ($\leq 3\%$ of Ag) while Shimakawa et al., [20] explained the same phenomena as a configurational entropy effect. We support the configurational entropy effect by assuming that at such low concentration of Ag, percolation does not occur. As stated earlier, this increase in diffusion in low Ag concentrated samples are due to an increase in configurational entropy, which we further confirm by the Raman analysis and discuss later. The increase in D as a function of Ag concentration in all samples were due to the decrease of $r_{\text{Ag-Ag}}$, i.e., steric hindrance between nearest Ag-Ag helps in diffusion, so the net effect in the increase of D but at low Ag content samples, as stated earlier – the fact that the lower the Ag concentration sample, Ag participates in bond

breaking and increasing of disorder in the structure, which increases the ionic interactions between a mobile ion (Ag^+) and the newly created Ge^- species, while higher Ag concentrated sample didn't show such phenomena i.e. breaking of homo-polar bond. This creates the net effect in reduction of D for the low Ag content ($\leq 1\%$) samples, however for the high Ag content ($\geq 1\%$) samples, as we stated earlier, the Ag plays a guest role in the GeSbSe host matrix. This is clear evidence of the dual role of Ag in these ionic conductors. Also, not only the behavior of D but also the magnitudes of D calculated using the RW model analysis are in good agreement with the D obtained from the tracer diffusion experiment done by Bychkov et al. [12] on same composition, as shown in Fig. 15b. This diffusion value (calculated by RW analysis) agreement with the experimentally obtained value (obtained by tracer diffusion) not only validate parameters calculated by the RW model analysis but also gives the chance to avoid the expensive and time consuming tracer diffusion method.

We also calculated N_{ions} as a function of temperature and found that the N_{ions} have almost constant magnitude as a function of temperature, i.e., temperature independent i.e. E_N (activation energy of mobile ions) ≈ 0 . At the same time, as Fig. 16 shows, the calculated D exponentially increased with temperature. The solid line in Fig. 16 represents the exponential fit, allowing the activation energy of diffusion (E_d) to be calculated as Fig. 17 shows.

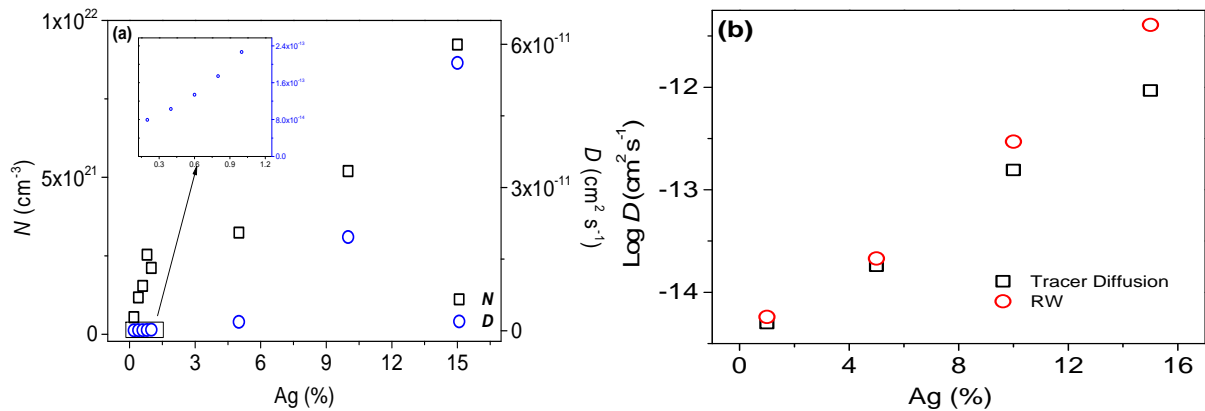


Fig. 15 (a) N_{ions} and D calculated using RW model fitting using Eqs. (6) and (7) at 368 K. (b) The diffusion coefficient calculated using the tracer diffusion method and RW model as a function of the Ag content at 298 K.

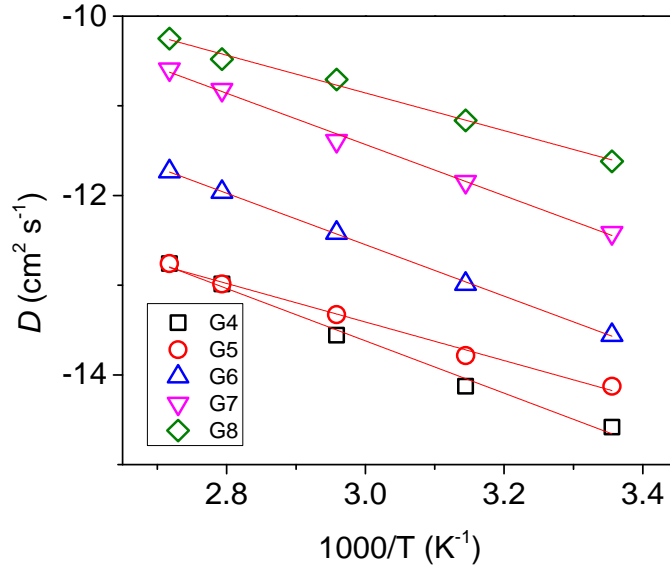


Fig. 16 The diffusion coefficient as a function of reciprocal of temperature. The solid line represents the exponential fit.

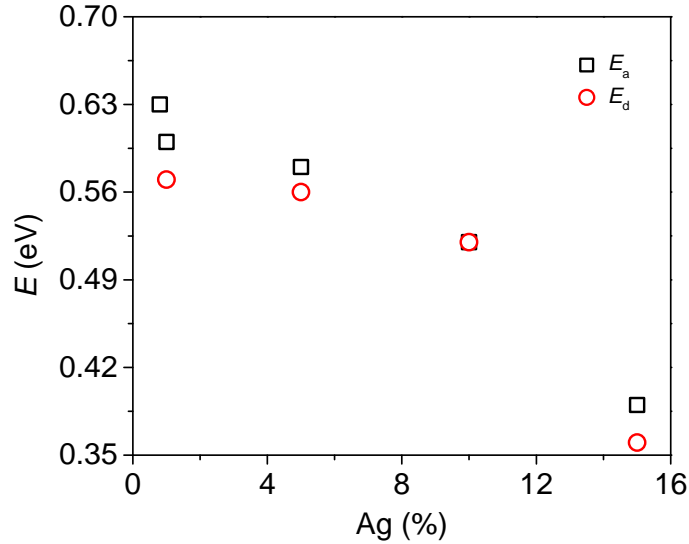


Fig. 17 A comparison of activation energy E_a with the diffusion activation energy E_d as a function of the Ag content.

The total activation (E_a) and the activation energy of diffusion (E_d) shown in Fig. 17, were in good agreement with each other, as we expected. Since, we stated above that the magnitude of $E_N \approx 0$ and we know,

$$E_a = E_N + E_d \quad (8)$$

where, E_N represents the activation energy of N_{ions} .

This means the activation energy in these samples were predominately governed by the diffusion coefficient.

3.7 Raman Analysis

In order to identify and correlate the structure with

the other properties of the materials, the Raman spectra of all prepared glasses $\text{Ag}_x(\text{Ge}_{28}\text{Sb}_{12}\text{Se}_{60})_{100-x}$ for $x = 0$ to 15, are presented in Fig. 18.

From Fig. 18, it can be observed that all the glasses including 0% Ag, i.e., pure $\text{Ge}_{28}\text{Sb}_{12}\text{Se}_{60}$ glass, have six fundamental characteristics peaks, i.e., at i) 160 cm^{-1} , ii) 170 cm^{-1} , iii) 195 cm^{-1} , iv) 203 cm^{-1} , v) 218 cm^{-1} and vi) the broad peak from $235\text{--}330 \text{ cm}^{-1}$. The peak at $\sim 170 \text{ cm}^{-1}$ corresponds to the stretching modes of the Ge-Ge homo-polar bonds in $[\text{Ge}_2\text{Se}_{6/2}]$ or $[\text{Ge}_{x/4}\text{-Ge-Se}_{(4-x)/2}]$ structural units presenting selenium deficiency. As Fig. 18 shows, the intensity of

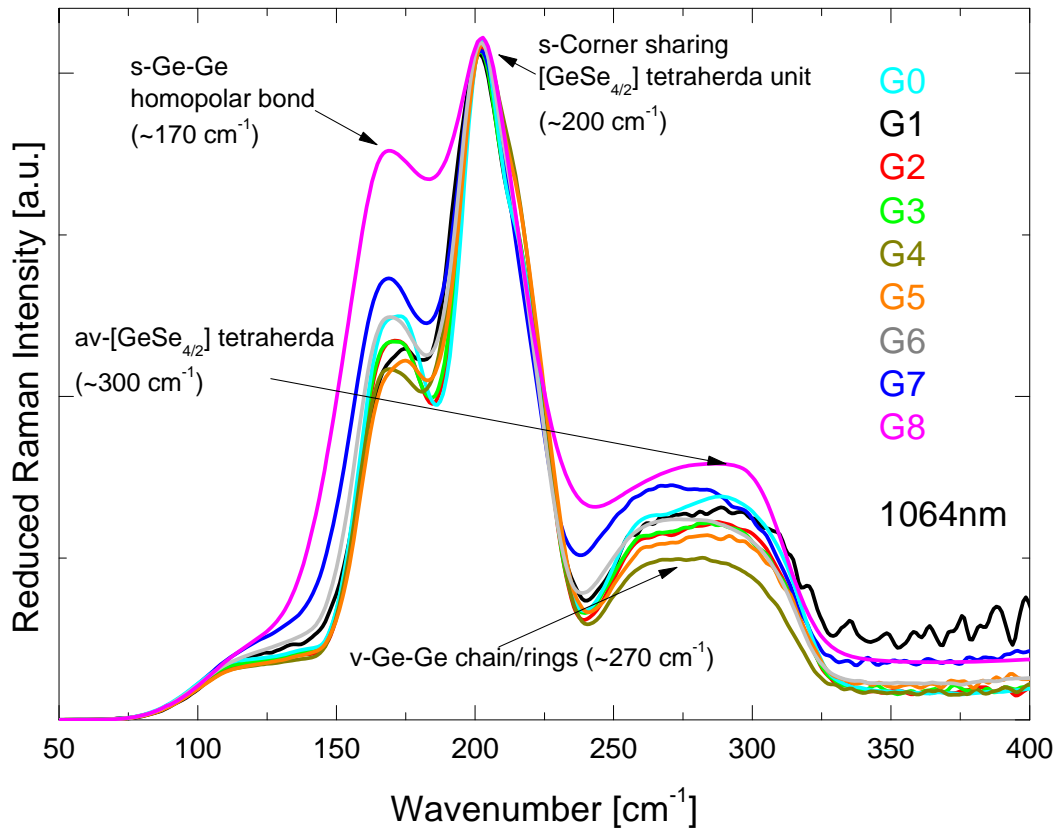


Fig. 18 The reduced Raman spectra of all glasses $\text{Ag}_x(\text{Ge}_{28}\text{Sb}_{12}\text{Se}_{60})_{100-x}$ having the excitation wavelength 1,064 nm.

the peak at $\sim 170 \text{ cm}^{-1}$ first decreases with the increase in the Ag content from 0 to 1% and further addition of Ag in our case $\geq 5\%$, the peak intensity started to increase and also shift towards 165 cm^{-1} , demonstrates, Ag has two different roles. The peak at $\sim 165 \text{ cm}^{-1}$ may be due to the stretching modes of the Sb-Sb homo-polar bond. These two different roles of Ag consistent with our earlier comment from optical, thermal and electrical properties as discussed in previous sections. The peak at 195 cm^{-1} represents the Sb-Se stretching mode, which is mostly overlapped with the peak at 203 cm^{-1} and not much influenced as a function of Ag content. The peak at 203 cm^{-1} represents the symmetric stretching mode connected by the corner sharing $[\text{GeSe}_{4/2}]$ tetrahedra unit. The absence of peak at 218 cm^{-1} due to a vibrational edge sharing $[\text{GeSe}_{4/2}]$ tetrahedra unit may have two possibilities, the first one is the less edge shared $[\text{GeSe}_{4/2}]$ tetrahedra unit which may be overlapped by

the peak at 203 cm^{-1} with the peak at 218 cm^{-1} , and the second possibility is a complete absence of an edge shared $[\text{GeSe}_{4/2}]$ tetrahedra unit. The second possibility is here more predominant due to the Se deficiency, due to a high Ge and Sb content, which is consistent with other author's observations [5, 21]. We can also observe that the peak intensity of the peak at 203 cm^{-1} is constant, i.e., there is no influence of the Ag addition on $[\text{GeSe}_{4/2}]$ tetrahedral unit in the structure. This clarifies that, Ag modifies the structure by making a rearrangement (i.e., bond breaking and making) through weak homo-polar bonds only. The broad peak at $235\text{--}330 \text{ cm}^{-1}$ actually represents several individual peak overlaps over each other, which could be assigned to i) the Ge-Ge bonds vibrations (in $\text{Ge}_x\text{GeSe}_{4-x}$, $x = 1, 2, 3, 4$ structural units) similarly to the amorphous germanium ($\sim 270 \text{ cm}^{-1}$), ii) the asymmetric vibration modes of $[\text{GeSe}_{4/2}]$ tetrahedra ($\sim 300 \text{ cm}^{-1}$). The peak at 300 cm^{-1} is consistent with our

earlier comment on the Se deficiency, also it has similar behavior as peak at $\sim 165\text{-}170\text{ cm}^{-1}$ i.e., its intensity decreased first in a lower Ag concentrated samples and at further addition of Ag it again started to increase. Here we would like to mention that the broad peak at $110\text{-}130\text{ cm}^{-1}$ is not much mentioned in literature [5, 21]. This peak is related to the Se-Se stretching mode [22] and it has many interesting features as a function of the Ag concentration, as we can observe in Fig. 18. The first thing is that the intensity of the peak $\sim 110\text{-}130\text{ cm}^{-1}$ first decreased with the Ag addition and at high percent of Ag i.e. $\geq 5\%$, the peak intensity again started to increase. This result is similar to other two peaks at $165\text{-}170\text{ cm}^{-1}$ and at $235\text{ - }330\text{ cm}^{-1}$, representing a correlation with homopolar bond modification. Also, the peak at $\sim 160\text{ cm}^{-1}$ is overlapped with the peak at $165\text{-}170\text{ cm}^{-1}$ and becomes broaden with increasing intensity, which reflects a new peak $\sim 150\text{ cm}^{-1}$ that may be attributed to a heteropolar Ge-Sb bond, as stated by Ivanova et al. [22], the possibility of the existence of the Ge-Sb heteropolar bond cannot be excluded.

From all these Raman spectral features, we can conclude that the Ag addition plays two different roles in modifying the $\text{Ge}_{28}\text{Sb}_{12}\text{Se}_{60}$ matrix structure, possibly at a low content of Ag, i.e., $\leq 5\%$, it reacts with Ge-Ge homopolar bonds and reduces the concentration of homopolar bonds in the matrix, which was confirmed by the decrease in peak intensities at 110 cm^{-1} , 170 cm^{-1} and the peak at 300 cm^{-1} . All these results were consistent with our previous section comments that, lower Ag concentrated samples, Ag participate in homopolar bond breaking and creating more disordered structure. As stated in earlier section, the electrode polarization tail was not observed even for a 15% Ag concentrated sample, this can be explained using the observation of the peak intensity variation of the peak at 170 cm^{-1} . The peak intensity increased as Ag content increased over 5%, indicating that Ag was not only just acting as a guest in the matrix empty space, but some of the Ag

absorbing Se (forming Ag_2Se) from the matrix, which further increase of Se deficiency and creating more homopolar Ge-Ge bonds. This is consistent with the peak intensity of the peak at 170 cm^{-1} , which is much more increased compared to G0 sample for high concentrated Ag. This is the reason for the lower ionic conductivity of these samples than the corresponding S-based samples. Also the increase of the Ge-Ge homopolar bond gives less pace is the reason for the decrease of the Ag-Ag atomic distance ($r_{\text{Ag-Ag}}$) and it can observe that from Fig. 6 the interlayer atomic distances ($\sim 5\text{ \AA}$). For higher concentrated Ag further breaking of Ge-Ge bonds and forming Ge^+ makes steric interaction much high, which cannot allow a stable structure, for this reason, Ag instead of breaking Ge-Ge homopolar started to absorb the Se atom from Ge of a distorted $[\text{GeSe}_{4/2}]$ tetrahedral structure and also from Sb of a distorted $[\text{SbSe}_{3/2}]$ pyramidal structure and formed more Ge-Ge and Sb-Sb homopolar bonds, which was confirmed by the increase in intensity of 110 cm^{-1} , 170 cm^{-1} , peak at 300 cm^{-1} and a new peak at $\sim 150\text{ cm}^{-1}$, $\sim 165\text{ cm}^{-1}$ respectively.

From all above characterizations, i.e., thermal, optical, electrical and structural, it is easy to conclude that the power law dependency of electrical conductivity in the lower Ag content ($\leq 5\%$) is due to role of Ag in structural modifications i.e. configurational entropy modification. This concentration-dependent Ag in structural modifications not only affects electrical properties but also thermal (T_g) and optical properties (E_g , n). It is also observed that the diffusion coefficient D obtained using the RW model analysis is in good agreement with the tracer diffusion experimental data, which gives further authenticity of the RW model and gives a versatile applicability to understand the electrical properties of disordered materials. Most importantly, the finding of the diffusion coefficient D using the RW model not only saves time but also avoids the use of the time consuming and very expensive tracer

diffusion technique (which uses radioactive elements).

4. Conclusions

In the present article, we systematically analyzed the prepared glasses $\text{Ag}_x(\text{Ge}_{28}\text{Sb}_{12}\text{Se}_{60})_{100-x}$ (where, $x = 0$ to 20), using different thermal, optical and electrical characterization techniques. Since, similar compositional study was already done by Bychkov et al., in the first part, we have shown the reproducibility of the obtained results and found that all the results are well reproducible. We observed density changes from $4.66 \text{ g}\cdot\text{cm}^{-3}$ to $5.48 \text{ g}\cdot\text{cm}^{-3}$ as Ag concentration changes from 0 to 15%. The $r_{\text{Ag-Ag}}$ distance decreased anomalously with an increase in the Ag concentration. The T_g of the samples also decreased in a similar manner. We also found that the materials transition from an insulating $\text{Ge}_{28}\text{Sb}_{12}\text{Se}_{60}$ (having conductivity in the order of $10^{-14} \text{ S}\cdot\text{cm}^{-1}$) to a fast ionic conductor for $\text{Ag}_{15}(\text{Ge}_{28}\text{Sb}_{12}\text{Se}_{60})_{85}$ (having conductivity in the order of $10^{-6} \text{ S}\cdot\text{cm}^{-1}$), i.e., the total conductivity changed by nine orders of magnitude. In the present article, the impedance data analysis is done by the RW model, and the diffusion coefficient D obtained using the RW model was compared with the experimental values obtained by the tracer diffusion method. We found good agreement with the experimental results. This not only authenticates the model data but also gives a valuable replacement for the expensive and time consuming tracer diffusion method. We have also correlated the parameters obtained from RW model with structural modifications. It was highlighted that the anomalous behavior of conductivity as well as T_g , E_g are due to the concentration-dependent dual behavior of Ag in the structure modification. In summary, this study helps to understand the ionic conduction in disordered/amorphous systems and gives an important contribution to the development of such ionic materials for various optoelectronic applications. Also, researchers can get benefits of calculating D of mobile ions directly from the impedance measurement i.e. the RW model can be

used as a preliminary technique for the analysis of D before going to use of the time consuming and expensive tracer diffusion method.

Acknowledgments

The authors would like to acknowledge the grant project CZ.1.07/2.3.00/20/0254 ReAdMat-Research Team for Advanced Non-Crystalline Materials realized by ESF, and Ministry of Education, Youth and Sports of the Czech Republic within ECOP, (Project KONTAKTII (CR-USA) LH14059 and grant LM2015082 Center of Materials and Nanotechnologies) for the financial support. Author Deepak Patil, would like to thank to the “Erasmus +” and “French Mobility Grant” programs for the financial support during the French stay and also would like to thank to Prof. Koichi Shimakawa and Prof. Miloslav Frumar for the discussion during the analysis of the current work.

References

- [1] Popescu, M. A. 2000. Non-Crystalline Chalcogenide, Kluwer Academic Publisher, Dordrecht, Netherlands.
- [2] Golovchak, R., Calvez, L., Petracovschi, E., Bureau, B., Savvitskii, D. and Jain, H. 2013. “Incorporation of Ga into the Structure of Ge-Se Glasses.” *Mater. Chem. Phys.* 138: 909-16.
- [3] Frumar, M. and Wagner, T. 2003. “Ag Doped Chalcogenide Glasses and their Applications.” *Curr Opin Solid ST. M.* 7: 117-26.
- [4] Hromadko, L., Prikryl, J., Strizik, L., Kostal, P., Benes, L. and Frumar, M. 2014. “Physico-Chemical Properties of Sb-Rich (Sb, In)-Te Thin Films.” *J. Alloy. Compd.* 617: 306-9.
- [5] Verger, F., Nazabal, V., Colas, F., Němec, P., Cardinaud, C. and Baudet, E. et al. 2013. “RF Sputtered Amorphous Chalcogenide Thin Films for Surface Enhanced Infrared Absorption Spectroscopy.” *Opt. Mater. Express* 3 (12): 2112-31.
- [6] Vitron. Spezialwerkstoffe GmbH. (www.vitron.de).
- [7] AMI. Amorphous Materials Inc. (www.amorphousmaterials.com).
- [8] Stehlik, S., Orava, J., Kohoutek, T., Wagner, T., Frumar, M. and Zima, V. et al. 2010. “Carbon Nanotube-Chalcogenide Glass Composite.” *J. Solid State Chem.* 183: 144-9.
- [9] Krbal, M., Stehlik, S., Wagner, T., Zima, V., Benes, L.

- and Frumar, M. 2007. "Electrical Properties and Structure of $\text{Ag}_x(\text{As}_{0.33}\text{S}_{0.335}\text{Se}_{0.335})_{100-x}$ Bulk Glasses." *J. Phys. Chem. Solids* 68: 958-62.
- [10] Mitkova, M., Sakaguchi, Y., Tenne, D., Bhagat, S. K., and Alford, T. L. 2010. "Structural Details of Ge-Rich and Silver-Doped Chalcogenide Glasses for Nanoionic Nonvolatile Memory." *Phys. Status Solidi A* 207 (3): 621-6.
- [11] Klein, R. J., Zhang, S., Dou, S., Jones, B. H., Colby, R. H. and Runt, J. 2006. "Modeling Electrode Polarization in Dielectric Spectroscopy: Ion Mobility and Mobile Ion Concentration of Single Ion Polymer Electrolytes." *J. Chem. Phys.* 124: 144903.
- [12] Bychkov, E., Tsegelnik, V., Vlasov, Yu., Pradel, A. and Ribs, M. 1996. "Percolation Transition in Ag-Doped Germanium Chalcogenide-Based Glasses: Conductivity and Silver Diffusion Results." *J. Non-cryst. Solids* 208: 1-20.
- [13] Tafen, D. N., Drabold, D. A. and Mitkova, M. 2005. "Silver Transport in $\text{Ge}_x\text{Se}_{1-x}$: Ag Materials: Ab initio Simulation of a Solid Electrolyte." *Phys. Rev. B* 72: 054206.
- [14] Patil, D. S., Shimakawa, K., Zima, V., Macak, J. and Wagner, T. 2013. "Evaluation of Impedance Spectra of Ionic-Transport Materials by a Random-Walk Approach Considering Electrode and Bulk Response." *J. Appl. Phys.* 113: 143705.
- [15] Patil, D. S., Shimakawa, K., Zima, V. and Wagner, T. 2014. "Quantitative Impedance Analysis of Solid Ionic Conductors: Effect of Electrode Polarization." *J. Appl. Phys.* 115: 143707.
- [16] Zima, V., Patil, D. S., Raja, D. S., Chang, T-G., Lin, C.-H. and Shimakawa, K. et al. 2014. "New MOF Based on Lithium Tetrahydrofuran-2,3,4,5-Tetracarboxylate: Its Structure and Conductivity Behavior." *J. Solid State Chem.* 217: 150-8.
- [17] Adam, J.-L. and Zhang, X. 2014. Chalcogenide Glasses: Preparation, Properties and Application, Woodhead Publishing Limited, 80 High Street, Sawston, Cambridge CB22 3HJ, UK.
- [18] Cui, S. 2014. "Synthesis and Characterization of Tellurium Based Glasses for Far Infrared Sensing and Thermoelectric Applications." Ph.D. thesis, Institute of Chemical Sciences, University of Rennes, Rennes, France.
- [19] Hubert, M. 2012. "Chalcogenide Glasses for Infrared Applications: New Synthesis Routes and Rare Earth Doping." Ph.D. thesis, The University of Arizona, Arizona, USA.
- [20] Shimakawa, K. and Wagner, T. 2013. "Origin of Power-Law Composition Dependence in Ionic Transport Glasses." *J. Appl. Phys.* 113: 143701.
- [21] Wei, W.-H., Wang, R.-P., Shen, X., Fang, L. and Luther-Davies, B. 2013. "Correlation between Structural and Physical Properties in Ge-Sb-Se Glasses." *J. Phys. Chem. C* 117 (32): 16571-6.
- [22] Ivanova, Z. G., Pamukchieva, V. and Vlcek, M. 2001. "On the Structural Phase Transformations in $\text{Ge}_x\text{Sb}_{40-x}\text{Se}_{60}$ Glasses." *J. Non-Cryst. Solids* 293-295: 580-5.